Bulletin of the Seismological Society of America

THE SEISMOLOGICAL SOCIETY OF AMERICA
400 Evelyn Ave., Suite 201
Albany, CA 94706-1375
(510) 525-5474; FAX (510) 525-7204
www.seismosoc.org

Bulletin of the Seismological Society of America, Vol. 104, No. 4, pp. 2027–2042, August 2014, doi: 10.1785/0120140015

An Attenuation Study of Body Waves in the South-Central Region of the Gulf of California, México

by Claudia A. Vidales-Basurto, Raúl R. Castro, Carlos I. Huerta, Danielle F. Sumy, James B. Gaherty, and John A. Collins

Abstract We studied the seismic attenuation of body waves in the south-central region of the Gulf of California (GoC) with records from the Network of Autonomously Recording Seismographs of Baja California (NARS-Baja), from the Centro de Investigación Científica y de Educación Superior de Ensenada's Broadband Seismological Network of the GoC (RESBAN), and from the ocean-bottom seismographs (OBS) deployed as part of the Sea of Cortez Ocean Bottom Array experiment (SCOOBA). We examine 27 well-located earthquakes reported in Sumy *et al.* (2013) that occurred from October 2005 to October 2006 with magnitudes (M_w) between 3.5 and 4.8. We estimated *S*-wave site effects by calculating horizontal-to-vertical spectral ratios and determined attenuation functions with a nonparametric model by inverting the observed spectral amplitudes of 21 frequencies between 0.13 and 12.59 Hz for the SCOOBA (OBS) stations and 19 frequencies between 0.16 and 7.94 Hz for NARS-Baja and RESBAN stations. We calculated the geometrical spreading and the attenuation ($1/Q$) factors for two distance intervals (10–120 and 120–220 km, respectively) for each frequency considered. The estimates of Q obtained with the SCOOBA (OBS) records for the interval 10–120 km indicate that the *P* waves attenuate more than *S* waves ($Q_P = 34 \pm 1.2f^{0.82\pm0.10}$, $Q_S = 59 \pm 1.1f^{0.90\pm0.03}$) for frequencies between 0.6 and 12.6 Hz; whereas for the 120–220 km interval, where ray paths travel deeper, *S* waves attenuate more than *P* waves ($Q_P = 117 \pm 1.3f^{0.44\pm0.19}$, $Q_S = 51 \pm 1.2f^{1.12\pm0.11}$). The estimates of Q obtained using NARS-Baja and RESBAN records, within 10–120 km, indicate that *P* waves attenuate more than *S* waves ($Q_P = 69 \pm 1.2f^{0.87\pm0.16}$, $Q_S = 176 \pm 1.4f^{0.61\pm0.26}$) at frequencies between 0.3 and 6.3 Hz; whereas at the 120–220 km distance interval *S* waves attenuate slightly more than *P* waves ($Q_P = 39 \pm 1.1f^{0.64\pm0.06}$, $Q_S = 48 \pm 1.1f^{0.37\pm0.07}$) at high frequencies ($f > 3$ Hz). These results, based on a unique OBS dataset, provide an indirect mean to constrain future models of the thermal structure beneath the GoC.

Introduction

The Gulf of California (GoC), Mexico, is composed of a series of pull-apart oceanic basins connected by transform faults, which strike in the northwest–southeast direction, consistent with Pacific–North America plate motion. The GoC was created 12 million years ago as a result of continental drift between the Pacific and North American plates (Karig and Jensky, 1972). Tectonically, the Baja California peninsula and the southern GoC are part of the Pacific plate, which is moving northwest relative to the North American plate, which contains the rest of Mexico (DeMets and Dixon, 1999; Plattner *et al.*, 2007; DeMets *et al.*, 2010). The modern-day boundary between these two plates is composed of short, nascent ridge centers connected by transform faults within the GoC (Thatcher and Brune, 1971; Suárez-Vidal *et al.*, 1991; Axen and Fletcher, 1998; Aragón-Arreola and Martin-Barajas, 2007).

The evolution of the GoC is related to different tectonic processes, which began with the subduction of the Farallón plate and followed by continental and oceanic rift processes (Stock and Hodges, 1989; Atwater and Stock, 1998; Axen *et al.*, 2000). Subsequently, the GoC was generated by the tectonic interaction of the Farallón, North America, and Pacific plates (Atwater, 1989; Martin-Barajas, 2000). From north to south, the GoC consists of basins formed by an oblique extensional system connected by right-lateral transform faults. The northern basins are shallow, whereas those in the central and southern region are deeper and are considered nascent spreading centers (Curray *et al.*, 1982). Most of the deformation in the northern GoC is generated by oblique faults with a lateral displacement component and by the transform faults in the southern region (Fenby and Gastil, 1991; Nagy and Stock,

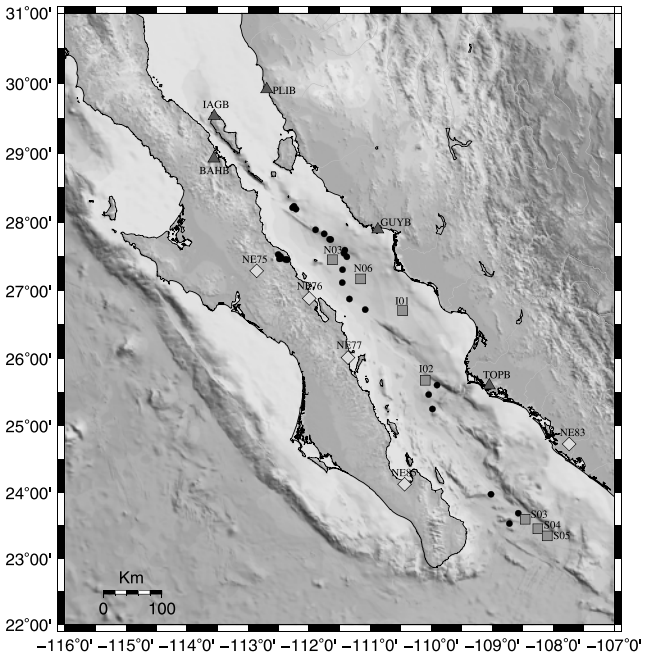

Figure 1. Map view of the 27 earthquakes (circles) recorded by the RESBAN (triangles), NARS-Baja (rhombuses), and SCOOBA OBS (squares) networks, respectively.

2000). The southern GoC is regarded as an area with high seismicity, because most of the earthquakes that are generated are related to these transform faults (Sumy *et al.*, 2013).

In October 2005, 15 ocean-bottom seismographs (OBS) were deployed as part of the Sea of Cortez Ocean Bottom Array (SCOOBA) experiment, a collaboration project between Centro de Investigación Científica y de Educación Superior de Ensenada (CICESE), Columbia University, and Woods Hole Oceanographic Institution (Sumy *et al.*, 2013). SCOOBA was designed to complement the onshore Network of Autonomously Recording Seismographs of Baja California (NARS-Baja) experiment operated by Utrecht University, Cal Tech, and CICESE to document seismicity within the GoC.

In this study, we analyze 27 events recorded by the NARS-Baja, RESBAN, and SCOOBA arrays to characterize the seismic attenuation of body waves in the south-central region of the GoC, Mexico. This is the first time OBS stations are used to study body-wave attenuation within the GoC, and the combined use of this unique dataset with the NARS-Baja and RESBAN dataset provides an improved travel-time resolution, particularly near the plate boundary.

We determine empirical attenuation functions that describe the spectral amplitude decay with distance at different frequencies (between 0.13 and 12.59 Hz) and then use these functions to estimate the quality factor Q for both P and S waves.

Data

We selected 27 earthquakes located by Sumy *et al.* (2013) and recorded simultaneously by stations of the NARS-Baja, RESBAN, and SCOOBA arrays (Fig. 1). These events have hypocentral distances between 10 and 220 km and magnitudes between 3.5 and 4.8. Figure 2 displays the distribution of earthquake magnitude versus hypocentral distance of the selected events. The NARS-Baja stations consist of Streckeisen STS-2 digital three-channel recorders with a built-in Global Positioning System (GPS) and 24-bit digitizer. The RESBAN stations consist of Güralp CMG-40T or CMG-3ESP digital three-channel recorders with a GPS and 24-bit Güralp digitizer. Both networks consist of three-channel stations of vertical, north–south, and east–west components of ground velocity. These broadband instruments are set to record earthquakes with a rate of 20 samples per second. The OBS stations are four-channel recorders (one channel for the vertical component of the ground motion [channel 3], two channels orthogonally oriented [channels 1 and 2] for the horizontal components, and a fourth channel for the pressure) sampling with a rate of 32.25 samples per second. The stations of the SCOOBA array consist of broadband seismometers provided by Scripps Institution of Oceanography.

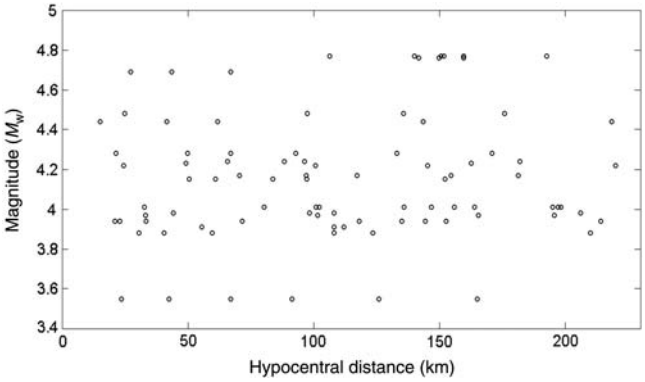

Figure 2. Spatial distribution of the seismograms used versus magnitude.

Figure 3 shows the seismograms of one earthquake recorded simultaneously by the SCOOBA, RESBAN, and NARS-Baja stations. The selected records were baseline corrected by subtracting the mean. We choose time windows containing clear P- and S-wave arrivals. We then calculate Fourier acceleration spectra of P- and S-wave signals using time window lengths of 4 s. The beginning and the end of the time windows were tapered with a 5% cosine taper before the Fourier transform was calculated. The spectral amplitudes were smoothed using a variable frequency band of ±25% over 21 predefined central frequencies between 0.13 and 12.59 Hz for OBS stations, and 19 frequencies, equidistant on a logarithmic scale, between 0.16 and 7.94 Hz for NARS-Baja and RESBAN stations (Table 1). The spectral amplitudes at the central frequency selected are the average amplitude within the corresponding frequency band. For further analysis, we visually inspected the spectral amplitudes to select frequency bands above the noise level. Figure 4 shows P- and S-wave acceleration spectra from the same event recorded at various hypocentral distances by the

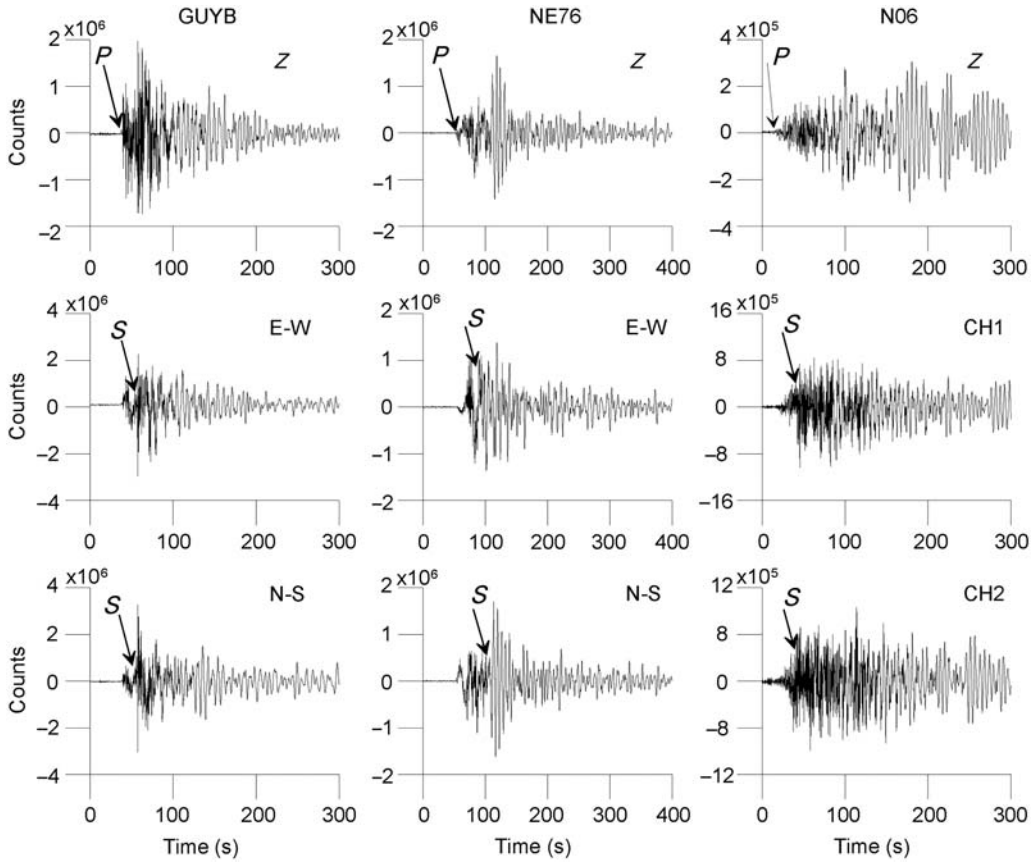

Figure 3. Sample seismograms from the earthquake that occurred on 4 January 2006 recorded at station GUYB (left column) of the RESBAN network, NE76 (central column) of the NARS-Baja array, and N06 (right column) of the SCOOBA array. Middle and bottom frames correspond to east–west (E–W) and north–south (N–S) components for stations GUYB and NE76, respectively. For the OBS station N06, middle and bottom frames are horizontal components, channel 1 (middle) and channel 2 (bottom).

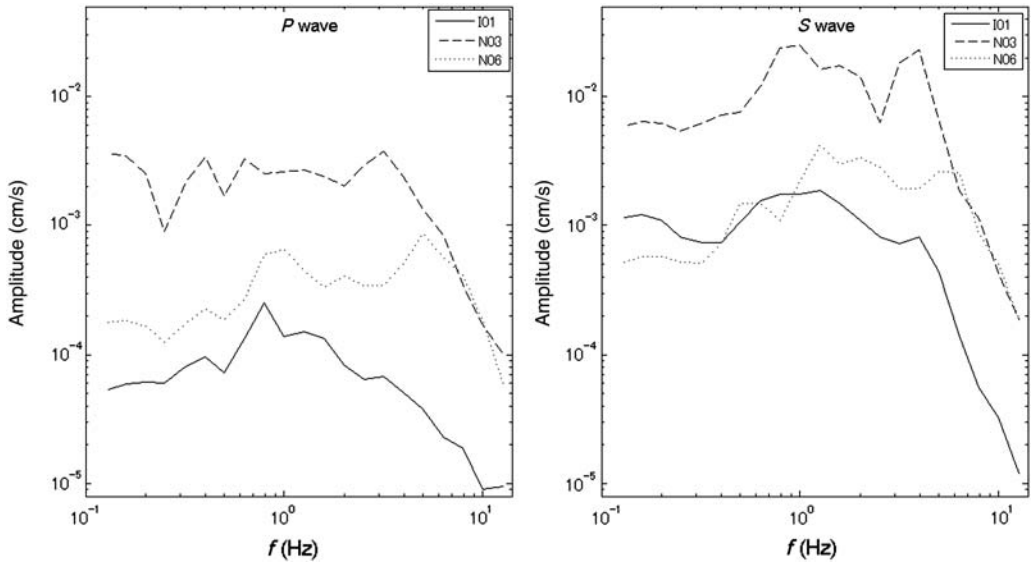

Figure 4. Body-wave acceleration spectra calculated from channel 1 (horizontal component) of the same earthquake recorded by OBS stations at 106.5 km (N03), 159.4 km (N06), and 243.5 km (I01). Left and right frames correspond to *P*- and *S*-wave spectra, respectively.

Table 1
Center Frequencies (f_c) and Frequency Band Used to Smooth the Spectral Amplitudes

f_c OBS (Hz)	f_c NARS-RESBAN (Hz)	f_1 (First Frequency)	f_2 (Last Frequency)
0.13		0.10	0.16
0.16	0.16	0.12	0.20
0.20	0.20	0.15	0.25
0.25	0.25	0.19	0.32
0.32	0.32	0.24	0.40
0.40	0.40	0.30	0.50
0.50	0.50	0.38	0.63
0.63	0.63	0.47	0.79
0.79	0.79	0.59	0.99
1.00	1.00	0.75	1.25
1.26	1.26	0.94	1.58
1.58	1.58	1.19	1.98
2.00	2.00	1.50	2.50
2.51	2.51	1.88	3.14
3.16	3.16	2.37	3.95
3.98	3.98	2.98	4.98
5.01	5.01	3.76	6.26
6.31	6.31	4.73	7.89
7.94	7.94	5.96	9.93
10.00		7.50	12.50
12.59		9.44	15.74

OBS stations. This figure shows how the spectral amplitudes decay considerably with distance for both body waves. For instance, the spectral amplitude at 1 Hz of the *P* wave (left frame in Fig. 4) is a factor of 18.6 greater at the station located at 106.5 km (N03) compared with that at the station at 243.5 km (I01), whereas for the *S* wave (right frame in Fig. 4) the spectral amplitudes at the same stations differ by a factor of 14.4. For this event the spectral amplitudes of the *P* wave decay more than the *S* wave. At $f < 1$ Hz the amplitudes of the acceleration spectra of stations I01 (at hypocentral distance of 243.5 km) and N06 (at 159.4 km) are similar in spite of the 84.1 km hypocentral distance difference, suggesting that station I01 must have important site amplifications at low frequencies.

Method

To characterize the attenuation of body waves in the GoC, we first calculated empirical attenuation functions using a nonparametric method (Anderson and Quaas, 1988; Castro *et al.*, 1990; among others). This method does not assume *a priori* a physical model; instead it finds attenuation functions that describe the observed spectral amplitude decay with hypocentral distance. The nonparametric model can be defined by the following equation:

$$U_i(r,f) = S_i(f)A(r,f), \tag{1}$$

in which $U_i(r,f)$ is the observed spectral amplitude at frequency f from event i recorded at hypocentral distance r, $S_i(f)$ is a scalar that depends on the size of the earthquake, and $A(r,f)$ is the empirically determined attenuation function that contains implicitly the effects of the geometrical spreading $G(r)$ and the quality factor Q. Thus, by comparing $A(r,f)$ with a physical model that explicitly considers $G(r)$ and Q, we retrieve these attenuation parameters in a second stage.

Equation (1) does not contain a site-effect term explicitly, so that the validity of the equation depends on eliminating this effect. The nonparametric method consists of finding a smooth function $A(r,f')$ at a frequency $f = f'$ assuming that the spectral amplitudes vary slowly with distance and that undulations in the data are related to site effects. Thus, site amplification effect is eliminated by constraining $A(r,f)$ to be smooth-decaying functions of distance. This method may not be adequate for regions where site amplification is stronger than attenuation or when site amplification increases with distance, because in these cases the observed amplitudes may not show clearly the amplitude decay with distance. Nevertheless, we estimated site effects with the horizontal-to-vertical spectral ratio (HVSR) method and corrected the observed spectral amplitudes for site effect before we calculated the attenuation functions with equation (1).

The nonparametric method also assumes that the rate of amplitude decay, governed by $A(r,f')$, is the same for all the earthquakes. The source factor $S_i(f')$ shifts upward or downward the attenuation function depending on the size of the event without modifying its shape. The advantage of this is that the observed amplitudes of events recorded at different distances at a given frequency complement each other and permits to define the attenuation function at a wider distance range (Castro *et al.*, 1990).

From equation (1), we formed at each frequency a set of linear equations described by

$$u_{ij} = s_i + a_j, \tag{2}$$

in which $u_{ij} = \log U_i(r,f)$ and is the datum from earthquake i recorded at distance j, $s_i = \log S_i(f)$, and $a_j = \log A(r,f)$, which is the value of the attenuation function at distance j.

Equation (2) represents an overdetermined system of equations that is solved by constrained least-squares inversion using multiple stations simultaneously and can be written in matrix form as

$$\mathbf{P}\vec{x} = \vec{m}, \tag{3}$$

in which $\vec{m}$ contains the observed spectral amplitudes, $\vec{x}$ contains the model parameters to be determined ($s_i = \log S_i(f)$ and $a_j = \log A(r,f)$), and the matrix $\mathbf{P}$ contains the constraints, so that, we obtain a solution consistent for the overdetermined system of equations. Equation (3) can be rewritten as

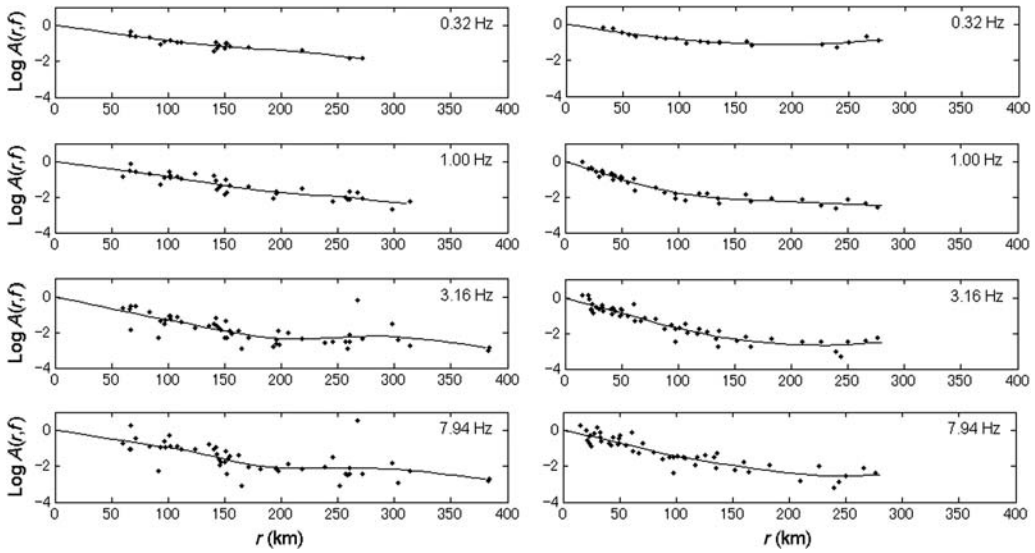

Figure 5. Examples of nonparametric attenuation functions obtained for four different frequencies. The dots are observed *P*-wave spectral amplitudes calculated from the earthquakes recorded between 60 and 384 km by NARS-Baja and RESBAN networks (left frames); and between 15 and 280 km by OBS stations (right frames).

$$\begin{bmatrix} 1 & 0 & 0 & 0 & 0 & & 1 & 0 & \\ 0 & 1 & 0 & 0 & 0 & \cdots & 1 & 0 & \cdots \\ 0 & 1 & 0 & 0 & 0 & & 0 & 1 & \\ & & \vdots & & & \ddots & & \vdots & \\ w_1 & 0 & 0 & 0 & 0 & & & & \\ -\frac{w_2}{2} & w_2 & -\frac{w_2}{2} & 0 & 0 & & & & \\ 0 & -\frac{w_2}{2} & w_2 & -\frac{w_2}{2} & 0 & \cdots & & \ddots & \\ 0 & 0 & 0 & \ddots & & & & & \\ & & \vdots & & & & & & \end{bmatrix} \begin{bmatrix} a_1 \\ \vdots \\ a_j \\ \vdots \\ a_{N_d} \\ s_1 \\ \vdots \\ s_i \\ \vdots \\ s_{N_{ev}} \end{bmatrix}$$

$$= \begin{bmatrix} u_{11} \\ \vdots \\ u_{ij} \\ \vdots \\ u_{N_e N_d} \\ 0 \\ 0 \\ 0 \\ 0 \\ 0 \end{bmatrix}, \qquad (4)$$

in which w_1 and w_2 are weighting factors used to constrain the attenuation functions to be 1 at $r = 0$ (spectral amplitudes are fully governed by the source term) and to weight the second derivative for smoothing purposes, respectively.

To find an adequate value of w_2, we looked for monotonic curves with a reasonable degree of smoothness. Figure 5 shows an example of the observed amplitudes and the attenuation functions obtained for *P* waves at four frequencies. The frames on the left of Figure 5 are the attenuation functions for *P* waves for earthquakes recorded by NARS-Baja and RESBAN, whereas the frames on the right correspond to *P* waves for earthquakes recorded by the OBS.

To test the validity of the site-effect assumption of the nonparametric method, we estimate *S*-wave site effects calculating spectral ratios between the horizontal and the vertical components of motion (HVSR), based on previous observations showing that the spectral amplitudes of the vertical component are relatively insensitive to site effects (Langston, 1977; Nakamura, 1989). Figure 6 displays the site response estimated using HVSR for OBS and on-land sites. The sites I01 and I02 (Fig. 6a) show the maximum amplification (up to 56 and 64, respectively) at 0.13 Hz for both horizontal components (channels 1 and 2). Because it is not possible to orient the horizontal components of the OBS in the north–south and east–west directions when they are installed, we will refer to these components for the recording channel number (channel 3 is the vertical component). The site response of I01 also shows peak amplifications, possibly related to higher modes of vibration, at 0.4, 1.0, and between 2.5 and 5.0 Hz. N03 has peak amplification factors that vary from 49 at 0.13 Hz to 13 at 3.2 Hz; N06 shows high amplification at low frequencies (near 0.13 Hz) and an amplification level of approximately 13 between 0.6 and 6.3 Hz; S03 has a peak amplification of 24 at 1.6 Hz and a comparatively low amplification (a factor of 5) at low frequencies ($f < 1.0$ Hz); at S04 the amplification seems to decrease with frequency from 21 at 0.13 Hz to 0 at 10 Hz; and S05 has two prominent amplification peaks, one near 1 Hz and

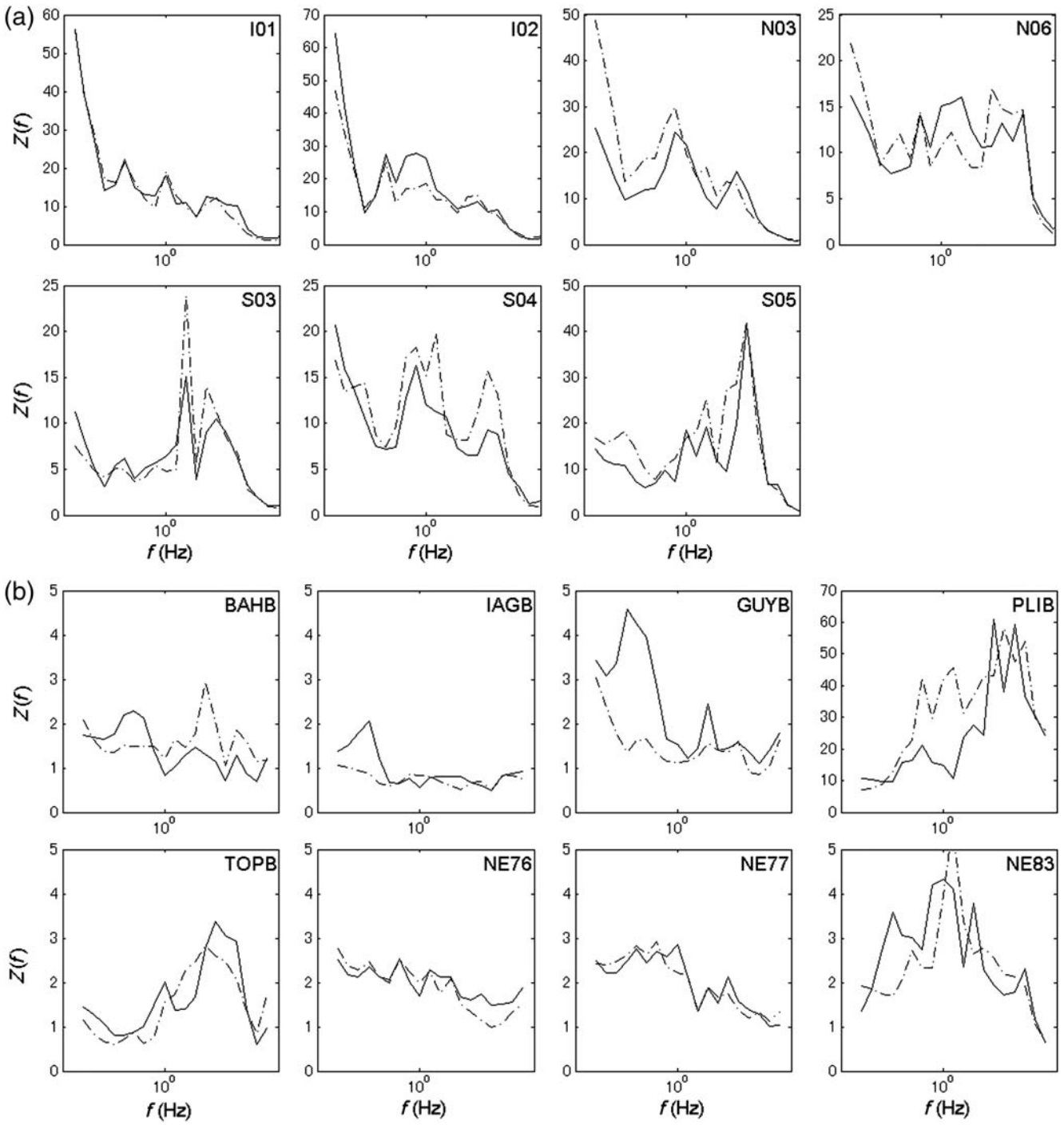

Figure 6. Spectral ratios between the horizontal and vertical components of ground motion (HVSR). (a) Site response of OBS sites; solid lines are used for one of the horizontal components (channel 1) and dotted lines for the other (channel 2). (b) Site response of stations located on land, dashed lines correspond to the north–south component and continuous lines for the east–west component.

another that reaches a factor of 22 at 5 Hz. It is likely that stations I01 and I02 are located on thicker sediments than the other stations, and that explains why the amplification is higher at low frequencies. S05, located at the southern extreme of the array shows peak amplification at higher frequencies (5 Hz) than the other sites, indicating that S05 is on more rigid rocks than the other sites. The stations located on land show smaller site amplifications (Fig. 6b) except for station PLIB that has an amplification factor up to 60 at high frequencies ($f > 1$ Hz). NE83 also shows important amplifications near 1 Hz, but the rest of the sites on land have, on average, amplification factors less than three.

Figure 7 shows attenuation functions of the *S* wave at four frequencies for earthquakes registered by the OBS

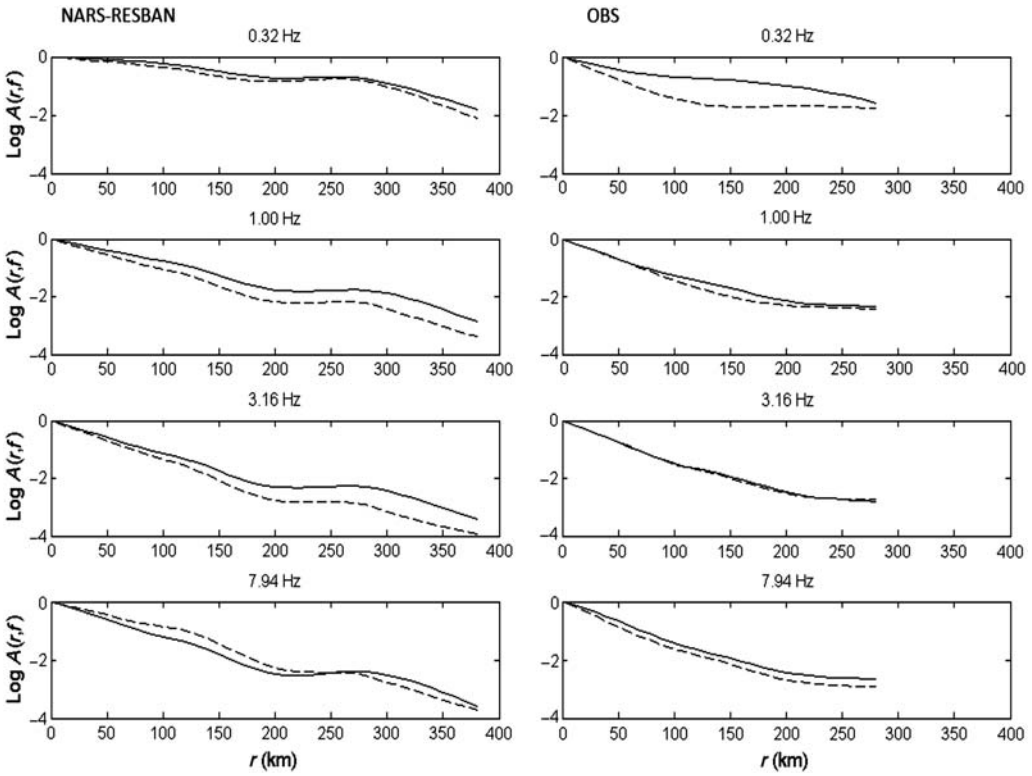

Figure 7. *S*-wave attenuation functions obtained using spectral amplitudes corrected (dashed lines) and uncorrected (solid lines) for sites effects at four different frequencies for earthquakes recorded by OBS stations (right frames) and by NARS-Baja and RESBAN stations (left frames).

stations (right frames) and the NARS-Baja and RESBAN stations (left frames). The dashed lines are attenuation functions obtained using spectral amplitudes corrected for sites effects, and the solid lines are attenuation functions obtained with uncorrected amplitudes. The difference between the corrected and uncorrected functions is minimal at 1.00, 3.16, and 7.94 Hz for the OBS stations, whereas for the NARS-Baja and RESBAN stations the difference is minimal at 0.32 and 7.94 Hz. In general, we observe little difference between the attenuation functions obtained with site-corrected spectral amplitudes and uncorrected amplitudes for distances less than 100 km.

The attenuation functions can be used to analyze various sources of attenuation and to estimate the quality factor Q at different frequencies f, assuming a homogeneous attenuation model of the form

$$A(r,f) = \frac{(N/r_0)}{(r/r_0)^n}\exp\left[\frac{-\pi f}{Qv}(r-N)\right], \qquad (5)$$

in which $A(r,f)$ is the attenuation function calculated at distance r, N is a normalization factor that corresponds with the minimum hypocentral distance of the data, $r_0 = 1$ km, which is a reference distance, v is the average velocity of the body wave, and $(N/r_0)/(r/r_0)^n$ is the geometrical spreading function. The attenuation of body waves can be characterized with the Q factor, which is a dimensionless and positive parameter ($Q > 0$). The value of Q depends on the seismic phase used and the elastic characteristics of the sampled region, and in equation (5) $1/Q$ is the total attenuation, which includes the effects of both intrinsic and scattering Q.

We observed that the inflection points of the different attenuation functions occur at different distances (Fig. 8), which suggests that the geometrical spreading may depend on both frequency and distance. In Figure 8, we show the empirical attenuation functions calculated for *P* and *S* waves at 18 frequencies between 0.25 and 12.59 Hz using OBS records. Although in theory $n = 1$ for body waves, we explore the significance of a possible frequency-dependent component of the geometrical spreading function by letting the exponent n free in equation (5).

Linearizing equation (5),

$$\log A(r,f) - \log N = -n\log r - \frac{\pi f}{Qv}\log e(r-N), \qquad (6)$$

in which the slope $m = \frac{\pi f \log(e)}{Qv}$ is estimated by least-squares fit (e.g., Castro *et al.*, 2003, 2004).

Equation (6) can be written as

$$J\vec{c} = \vec{d}, \qquad (7)$$

in which $\vec{d} = \log A_j(r,f) - \log N$, $\vec{c}$ contains the parameters to determine, which are the exponent of geometrical spreading (n) and the attenuation factor $(1/Q)$, and $J = -\log r_j - \frac{\pi f}{v}\log e(r_j - N)$.

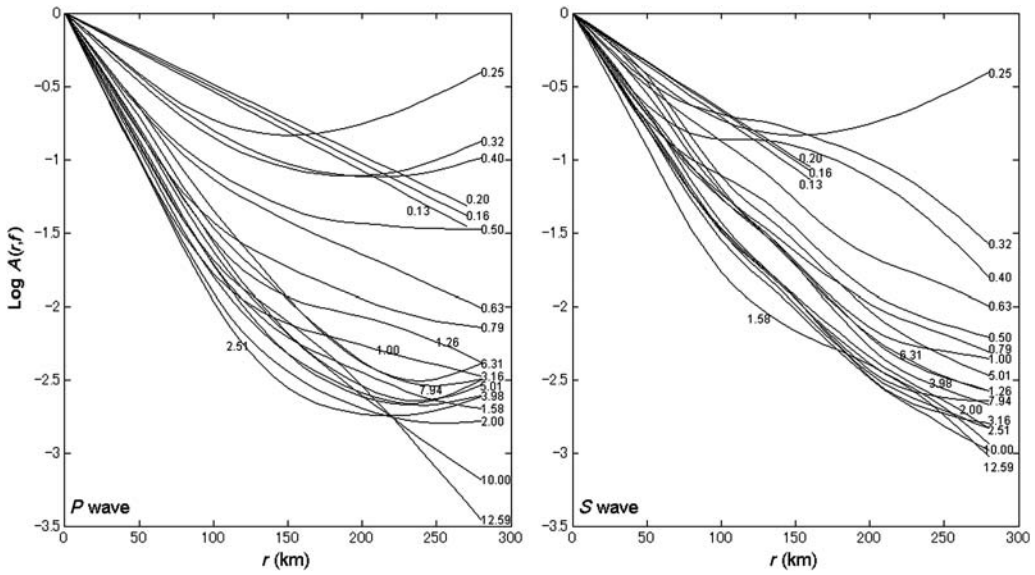

Figure 8. *P*- and *S*-wave attenuation functions obtained at 18 frequencies between 0.25 and 12.59 Hz using spectral records from all OBS stations. The curves have inflexion points at different distances for both *P* waves (left frame) and *S* waves (right frame).

Equation (7) represents an overdetermined system of equations, and we can rewrite it as

$$\begin{bmatrix} d_1 \\ d_2 \\ \vdots \\ d_j \end{bmatrix} = \begin{bmatrix} -\log r_1 & -\frac{\pi f \log e}{v}(r_1 - N) \\ -\log r_2 & -\frac{\pi f \log e}{v}(r_2 - N) \\ \vdots & \vdots \\ -\log r_j & -\frac{\pi f \log e}{v}(r_j - N) \end{bmatrix} \begin{bmatrix} n \\ \frac{1}{Q} \end{bmatrix}. \quad (8)$$

We solved this system of equations for each f considered with a singular value decomposition scheme (Menke, 1984).

To describe the observed frequency dependence of the estimated values of Q, we use the functional form

$$Q = Q_0(f/f_0)^a, \quad (9)$$

in which Q_0 is the value of Q at $f_0 = 1.00$ Hz.

To quantify the seismic attenuation in the south-central region of the GoC, we estimated Q factors with the attenuation functions obtained between 0.13 and 12.59 Hz with the SCOOBA stations and between 0.25 and 7.94 Hz obtained with NARS-Baja and RESBAN stations. The frequency bands are slightly different because the low-frequency signal-to-noise ratio and the sampling rate (Nyquist frequency) are different. We choose two distance intervals defined by the changes in the curvature of the attenuation functions to estimate Q, one interval between 10 and 120 km and another between 120 and 220 km.

Results and Discussion

We show (Fig. 6) that the resulting site response functions obtained by calculating the average HVSR for seven OBS stations deployed on the seafloor near the boundary between the Pacific and North America plates have important amplifications. For instance, stations I01 and I02 have amplification factors up to 65 times at low frequencies. We also calculated HVSR using the stations located on the Baja California Peninsula (stations from the NARS-Baja and RESBAN arrays). The main features of the site response are the expected low relative amplification at rock sites and high amplification at soft sites. The peak amplification factors for the OBS stations range between 5 and 65 from site to site (Fig. 6) and are higher than the peak amplification factors calculated for the NARS-Baja and RESBAN sites. We used the site-effect functions to correct the observed spectral amplitudes, and we used the corrected amplitudes to determine attenuation functions for *S* waves. There are, in general, few differences between the attenuation functions obtained with site-corrected spectral amplitudes and those obtained with uncorrected amplitudes for short distance ranges ($r < 100$ km) (Fig. 7).

The extensional tectonics within the GoC results in a thinner crust near the plate boundary (González-Fernández *et al.*, 2005; Lizarralde *et al.*, 2007), and, thus, we expect seismic attenuation to increase near the ridge-transform fault system. We tested this hypothesis by calculating the empirical attenuation functions for *P* and *S* wave paths recorded by the OBS stations within the GoC (Fig. 9) and for paths that sample the continental margins with NARS-Baja and RESBAN records (Fig. 10). For both cases, the resulting empirical attenuation functions (Fig. 7) decay faster with increasing frequency, particularly for paths that approach the boundary between the North America and Pacific plates (Fig. 9 and right column of Fig. 7), where there is more seismic activity, the thickness of the crust is thinner, and new ocean floor is being created.

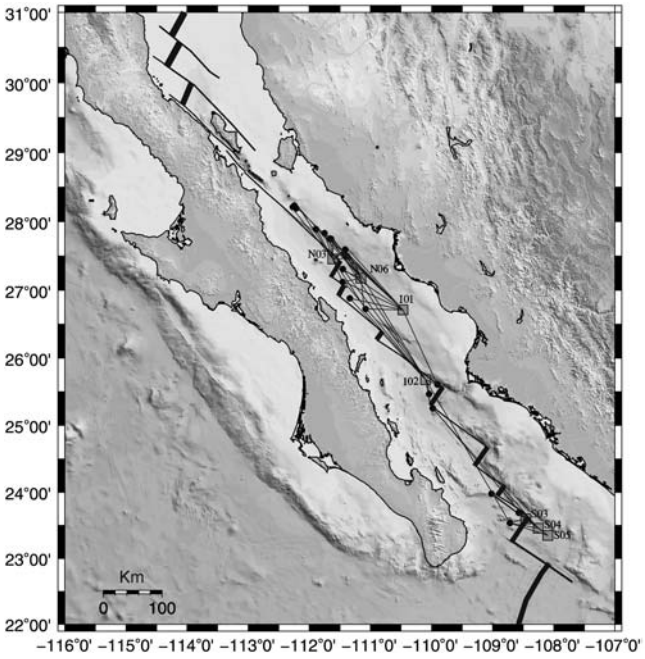

Figure 9. Map showing source–station paths of the earthquakes recorded by OBS stations.

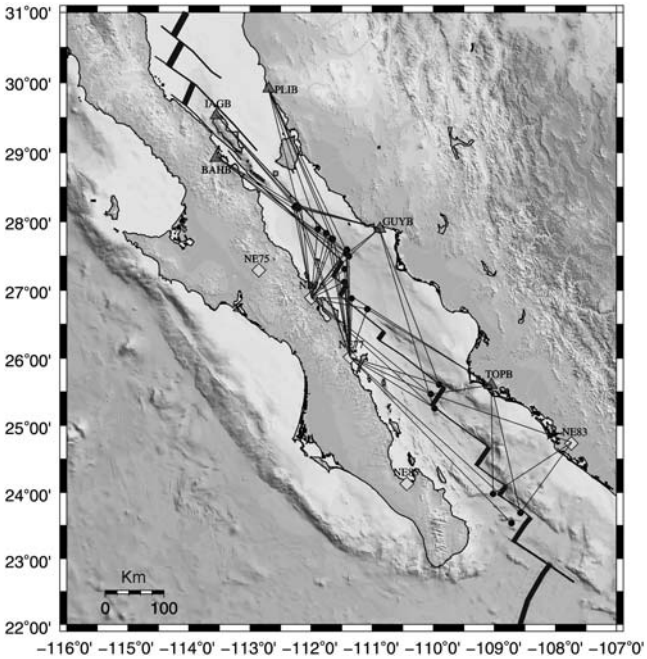

Figure 10. Map showing source–station paths of the earthquakes recorded by RESBAN and NARS-Baja stations.

The estimates of Q, obtained by solving equation (8), are also a powerful tool to quantify the tectonic activity of the GoC. Previous studies of Q (Singh and Herrmann, 1983; Hasegawa, 1985) indicate that in areas with low attenuation, low seismicity, and thick crust, Q_0 tends to have very high values, whereas the exponent a (equation 9) tends to be very low (between 0.2 and 0.4). The opposite occurs in regions with high seismicity, where the seismic-wave velocity decreases due to the presence of young, thin crust and/or high heat flow. In these regions, Q_0 values tend to be low ($\leq$100), whereas $a > 1$, which indicates high inelastic attenuation of the tectonic environment.

For the OBS stations, we estimate the P-wave attenuation factor $(1/Q)$ with the corresponding error (Fig. 11, left frame) and the least-squares fit of Q (Fig. 11, right frame) for 10–120 km (triangles) and 120–220 km (circles) distance intervals in the 0.63–12.59 Hz frequency band. We fit the Q estimates to equation (9) and obtain $Q_P = 34 \pm 1.2f^{0.82\pm0.10}$ and $Q_P = 117 \pm 1.3f^{0.44\pm0.19}$ for distances between 10–120 and 120–220 km, respectively.

Similarly, we estimate the S-wave attenuation factor $(1/Q)$ with the respective error bars (Fig. 12, left frame) and the least-squares fit of Q (Fig. 12, right frame) for 10–120 km (triangles) and 120–220 km (circles) distance intervals in the 0.13–12.59 Hz frequency band. The dependence of Q on frequency can be approximated with the relations $Q_S = 59 \pm 1.1f^{0.90\pm0.03}$ and $Q_S = 51 \pm 1.2f^{1.12\pm0.11}$ for distances between 10–120 and 120–220 km, respectively.

For the NARS-Baja and RESBAN stations, we estimate the P-wave attenuation factor $(1/Q)$ with the corresponding error bars (Fig. 13, left frame) and the least-squares fit of Q (Fig. 13, right frame) for 10–120 and 120–220 km distance intervals. In the 0.3–7.9 Hz frequency band, we find that $Q_P = 69 \pm 1.2f^{0.87\pm0.16}$ and $Q_P = 39 \pm 1.1f^{0.64\pm0.06}$ for distances between 10–120 and 120–220 km, respectively.

Similarly, we estimate the S-wave attenuation factor $(1/Q)$ with error bars (Fig. 14, left frame) and the least-squares fit of Q (Fig. 14, right frame) for 10–120 and 120–220 km distance intervals in the 0.25–6.31 Hz frequency band for S waves recorded by NARS-Baja and RESBAN stations, in which $Q_S = 176 \pm 1.35f^{0.61\pm0.26}$ and $Q_S = 48 \pm 1.07f^{0.37\pm0.07}$ for distances between 10–120 and 120–220 km, respectively.

The values of the geometrical spreading exponent (n) obtained by solving equation (8) for different frequencies are shown in Figure 15. At short distances (10–120 km), n varies between 0.8 and 1.1 for P waves (triangles on Fig. 15a) and between 0.8 and 1.0 for S waves (Fig. 15b). For longer hypocentral distances (120–220 km), n shows bigger variability with frequency (circles in Fig. 15), taking values between 0.5 and 1.6 for P waves and between 0.25 and 1.2 for S waves. These results suggest that the geometrical spreading has weak frequency dependence at short distances (10–120 km), for both P and S waves, and a more complex behavior at longer distances where direct, refracted, and reflected waves interact. Because the geometrical spreading is controlled by the crustal structure, it is expected that the source–station paths of the OBS data, which are near the ridge transform faults, have different geometrical spreading parameters compared with the source–station paths of the NARS-RESBAN stations. Although the model parameter n estimated for the short distance interval is very similar for

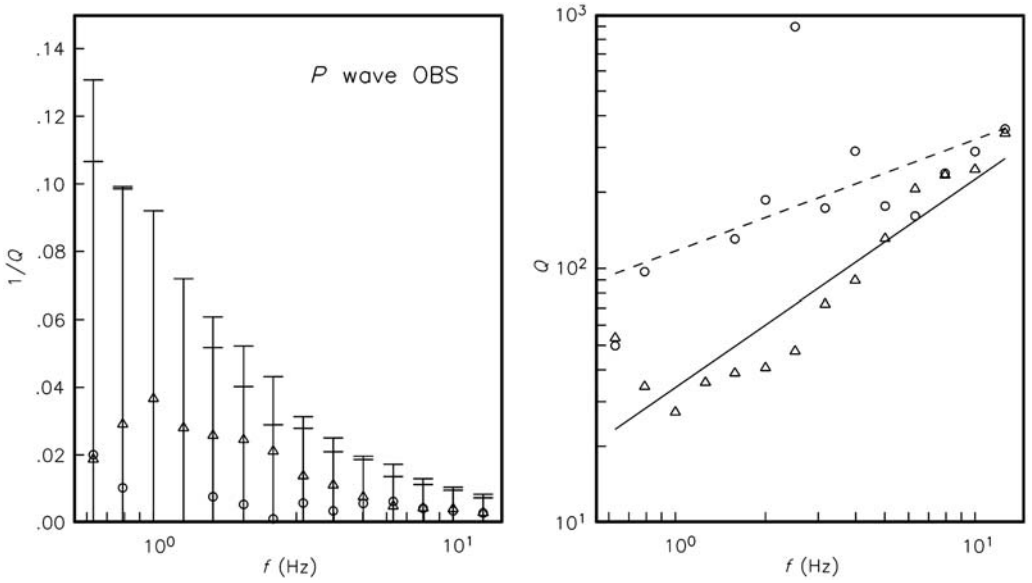

Figure 11. Estimates of $(1/Q) \pm 1$ standard deviation (left frame) and *P*-wave Q (right frame) recorded by OBS. The triangles correspond to paths of 10–120 km and circles to the hypocentral distances between 120 and 220 km.

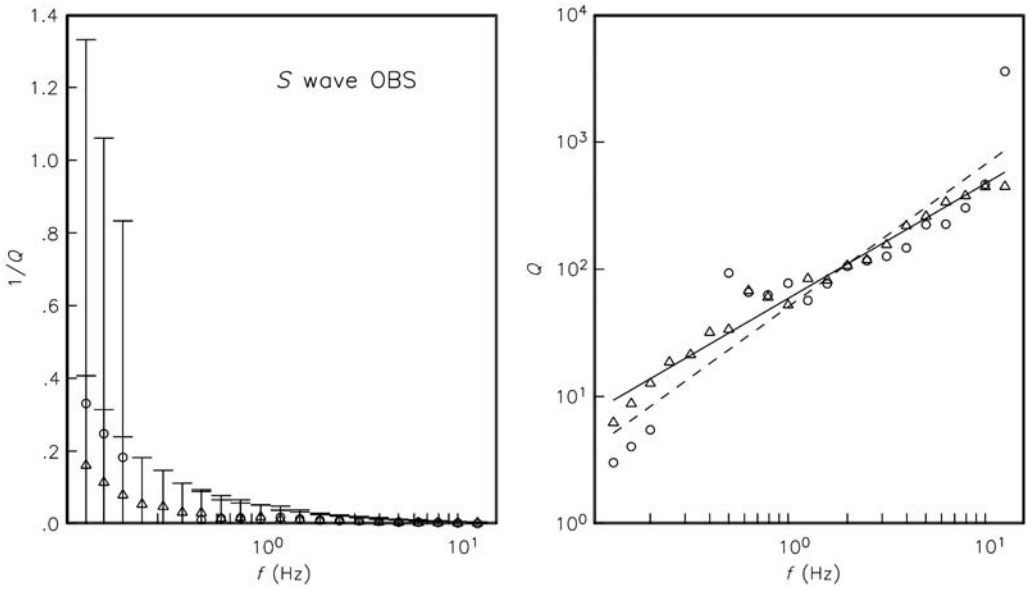

Figure 12. Estimates of $(1/Q) \pm 1$ standard deviation (left frame) and *S*-wave Q (right frame) recorded by OBS. The triangles correspond to paths of 10–120 km and circles to the hypocentral distances between 120 and 220 km.

both source–station paths (Fig. 15), for the 120–220 km interval n tends to have higher values for the OBS source–station paths. Figure 16, modified from Lizarralde *et al.* (2007), summarizes the differences between the crustal structure at the margins and within the GoC. On the margins the crust is thicker and the body-wave velocity of shallow layers faster than along the plate boundary within the GoC, where the OBS stations were installed.

The attenuation characteristics of the GoC, quantified with Q, can be related with the crustal structure and the tectonic evolution of this region. The formation of the GoC extensional province occurred in two phases: in the first stage the extension and continental separation formed continental marine basins, whereas during the second phase, a period of seafloor expansion and creation of transform faults took place, and these latter processes continue today (Stock and Hodges, 1989; Oskin *et al.*, 2001; Bennett *et al.*, 2007). As a consequence, the crustal structure at the margins of GoC is different with respect to the crustal structure along the plate boundary within the GoC (Fletcher and Munguía, 2000). The estimates of Q for *S* waves (Figs. 12 and 14) show that paths sampling the Baja California Peninsula region in the

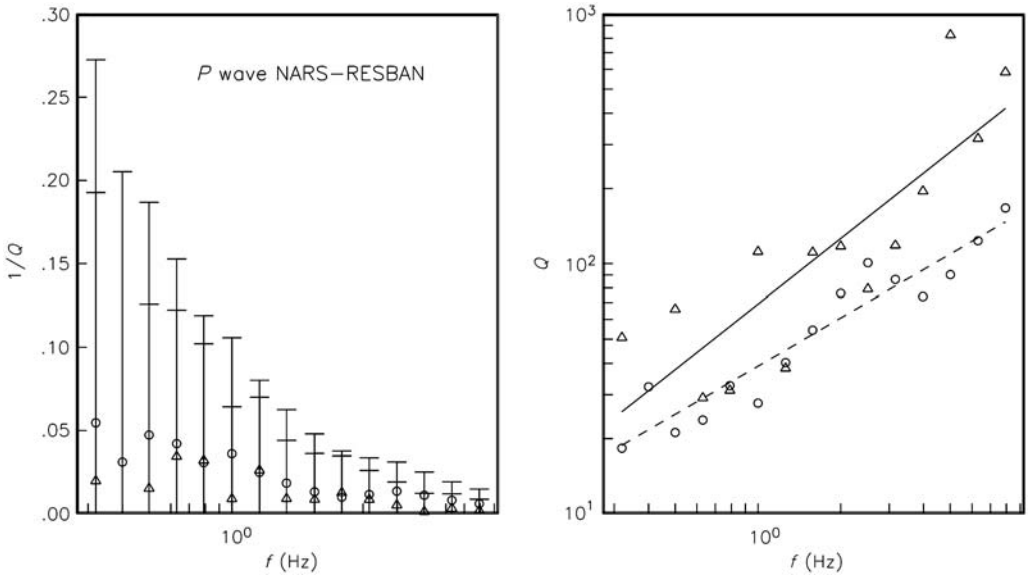

Figure 13. Estimates of $(1/Q) \pm 1$ standard deviation (left frame) and P-wave Q (right frame) recorded by NARS-Baja and RESBAN networks. The triangles correspond to paths of 10–120 km and circles to the hypocentral distances between 120 and 220 km.

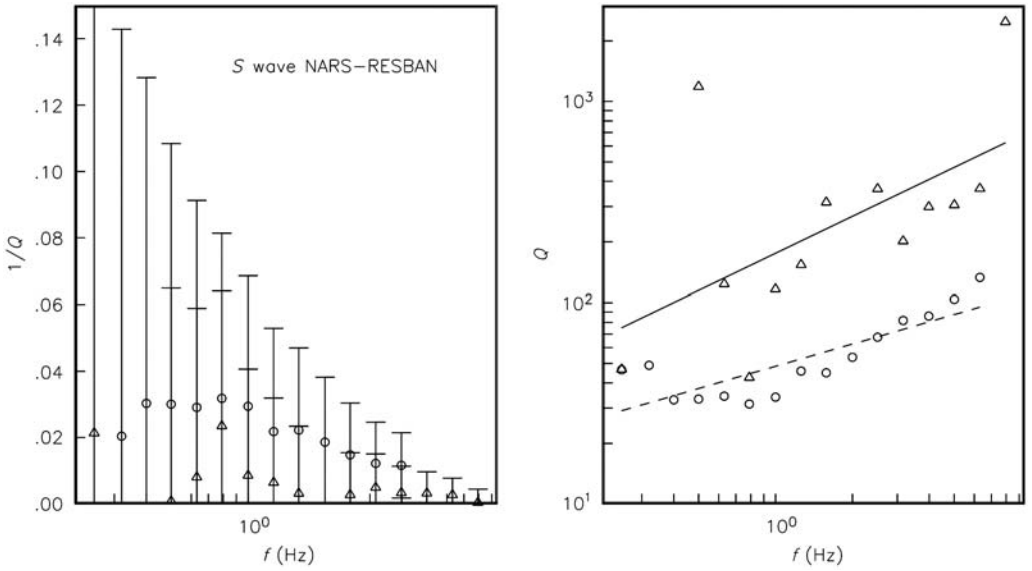

Figure 14. Estimates of $(1/Q) \pm 1$ standard deviation (left frame) and S-wave Q (right frame) recorded by NARS-Baja and RESBAN networks. The triangles correspond to paths of 10–120 km and circles to the hypocentral distances between 120 and 220 km.

10–120 km interval present higher values ($Q_S = 176f^{0.61}$) than paths recorded by the OBS stations within the GoC ($Q_S = 59f^{0.90}$). This finding reflects the resistance of crustal rocks to fracture (e.g., Hough and Anderson, 1988) near the Baja California Peninsula when compared with regions near the GoC spreading centers, where the heat flux increases, the speed of the waves decreases and thus the value of Q must be comparatively small.

The S-wave Q factor obtained with records from the NARS-Baja and RESBAN stations between 120 and 220 km distances ($Q_S = 48f^{0.37}$) contains paths that traveled near the plate boundary, which are similar to the paths of the OBS records ($Q_S = 51f^{1.12}$).

Attenuation is a physical parameter very sensitive to high temperatures and saturation of rocks with fluids and partial melting (Haberland and Rietbrock, 2001). Therefore, the relationship Q_P/Q_S is a better indicator of rock-fluid content than the velocity ratio V_P/V_S (Winkler and Nur, 1979). We examine the Q_P/Q_S ratio as a function of frequency (Fig. 17) calculated from the Q values shown in Table 2. For OBS records within the 10–120 km distance interval, where the waves travel at shallow depths, the crust

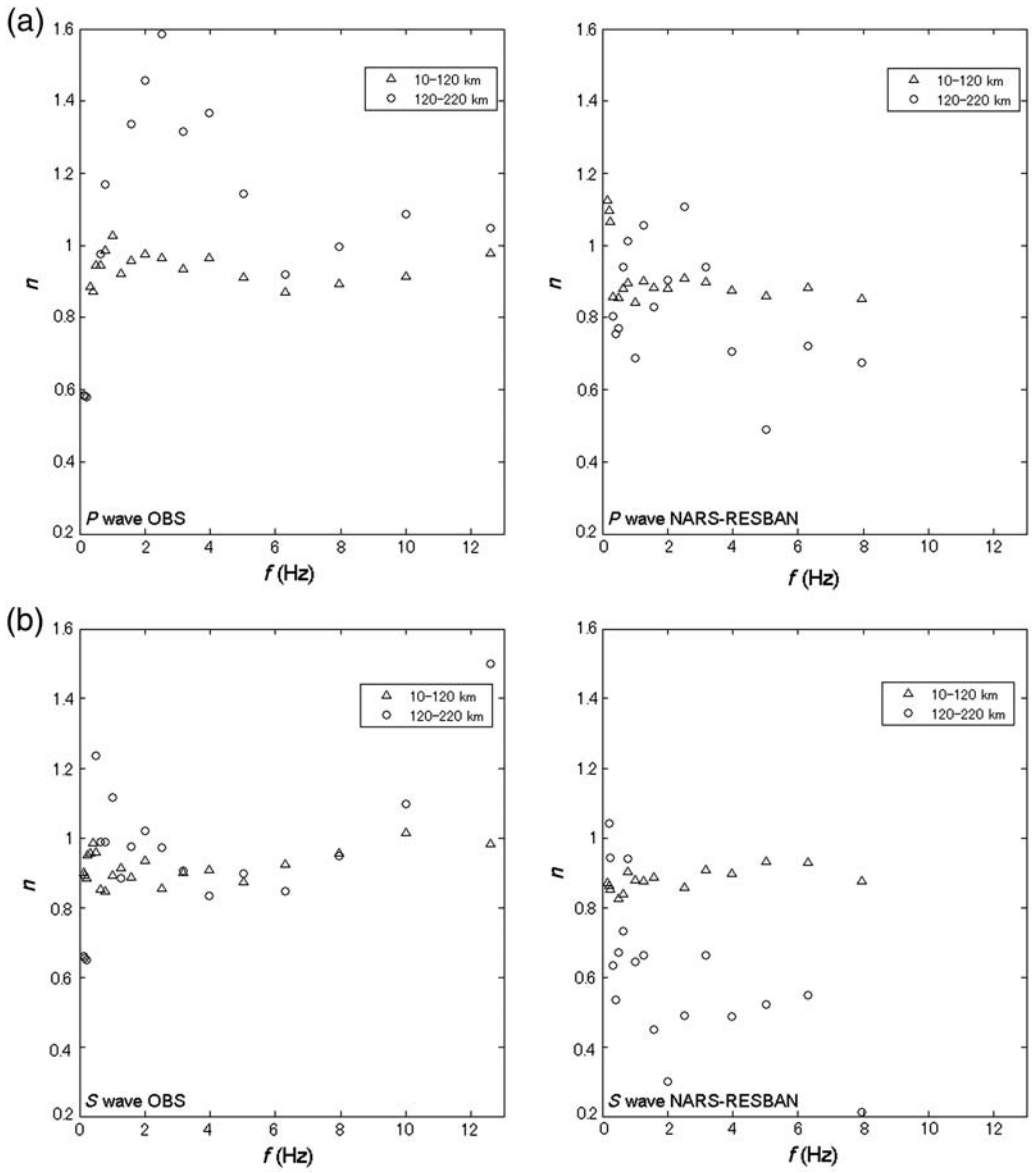

Figure 15. Dependence between the exponent of geometrical spreading n and frequency found (a) for P waves and (b) for S waves recorded by OBS (frames on the left), and NARS-Baja and RESBAN networks (frames on the right). Triangles correspond to earthquakes in the hypocentral distance interval 10–120 km and circles for the 120–220 km interval.

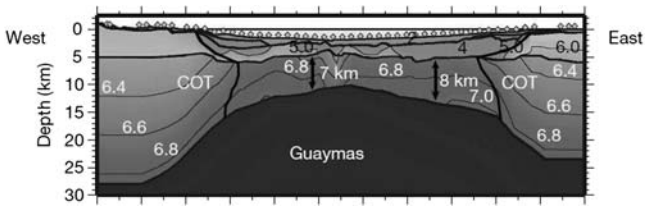

Figure 16. Crustal structure model obtained by Lizarralde *et al.* (2007) along the Guaymas basin (where the OBS stations in this paper were installed). The P-wave velocity contours are in kilometers per second. The model was determined using a forward/inverse travel-time technique.

contains microcracks, and the rocks are fluid saturated (e.g., Johnston *et al.*, 1979; Winkler and Nur, 1982), we find that P waves attenuate more than S waves for frequencies between 0.6 and 12.6 Hz. On the contrary, we find for the 120–220 km interval (for deeper travel paths) that S waves attenuate more than P waves up to 3.5 Hz, indicating that in the lower crust and upper mantle the temperature must be higher and the rocks probably less fractured. At higher frequencies ($f > 3.5$ Hz) P waves attenuate more than S, for the 120–220 km interval, probably due to changes in the degree of saturation of the rocks. Experimental studies of seismic-wave attenuation in rocks show that when the rocks are partially

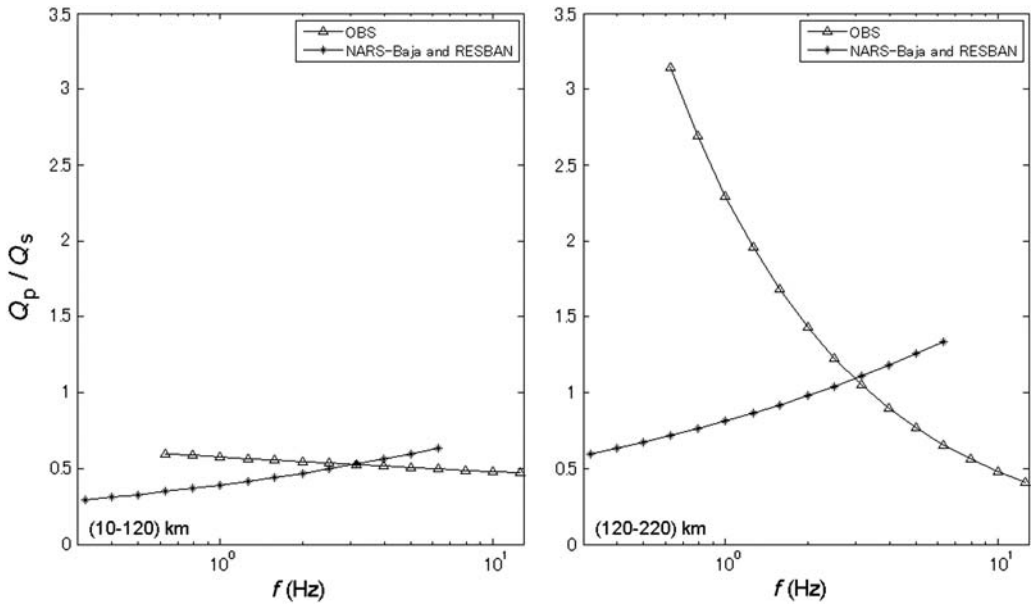

Figure 17. Q_P/Q_S ratios calculated from the Q values shown in Table 2.

saturated $(Q_P/Q_S) < 1$ and that $(Q_P/Q_S) > 1$ for total saturation (Winkler and Nur, 1982). Q_P/Q_S ratio also permits to infer the attenuation mechanisms, for instance, Sato (1984) found that $(Q_P/Q_S) = 0.42$ for Rayleigh scattering at high frequencies and in general is expected that $Q_P/Q_S \leq 1$ for most kinds of scattering (Hough and Anderson, 1988). The complex crustal structure of the GoC can be the principal source of scattering. Based on seismic and gravity modeling, González-Fernández *et al.* (2005) found that in the GoC the crustal thickness has important variations and this must generate complex wave propagation effects, including body-wave scattering.

The estimates of Q obtained with NARS-Baja and RESBAN records within 10–120 km indicate that P waves attenuate more than S waves between 0.3 and 6.3 Hz and between 0.3 and 2.0 Hz within the 120–220 km distance range (Fig. 18, upper right frame). The estimates of Q determined with OBS data (upper left frame in Fig. 18) also show a similar trend, $Q_P < Q_S$ at the short distance range and at high frequencies ($f > 3$ Hz) for longer distances (120–220 km). At low frequencies ($f < 3$ Hz) and longer distances (120–220 km), however, $Q_P > Q_S$. At low frequencies ($f < 3$ Hz) and deeper ray paths (within the 120–220 km hypocentral distance range) S waves attenuate more than P waves, near the plate boundary, probably by the temperature increase with depth and a stronger scattering effect. The estimates of Q obtained for the 10–120 km distance range with OBS records are in general smaller than those obtained with the RESBAN-NARS stations (lower frames in Fig. 18 and Table 2). These results agree with other attenuation studies made in the Pacific Ocean region where it has been observed that inelastic attenuation depends on lithospheric age, being higher (lower Q) for young lithosphere (Tsai and Aki, 1969; Mitchell *et al.*, 1976; Canas and Mitchell, 1978). The opposite occurs for waves traveling the longer distance range (120–220 km) where our estimates of Q (lower frames in Fig. 18) obtained with OBS records tend to be higher than those obtained with the mixed ray paths of the RESBAN-NARS stations that travel though crustal structures with more pronounced lateral variations.

Conclusions

The nonparametric attenuation functions obtained for the south-central region of the GoC illuminate how seismic-

Table 2
Estimates of Q Obtained for P (Q_P) and S (Q_S) Waves at Different Distance Intervals

	10–120 km	120–220 km	Frequency Band (Hz)
OBS	$Q_P = 34 \pm 1.2 f^{0.82\pm0.1}$	$Q_P = 117 \pm 1.3 f^{0.44\pm0.19}$	0.63–12.59
	$Q_S = 59 \pm 1.1 f^{0.9\pm0.03}$	$Q_S = 51 \pm 1.2 f^{1.12\pm0.11}$	0.13–12.59
RESBAN–NARS Baja	$Q_P = 69 \pm 1.2 f^{0.87\pm0.16}$	$Q_P = 39 \pm 1.1 f^{0.64\pm0.06}$	0.32–7.94
	$Q_S = 176 \pm 1.4\ f^{0.61\pm0.26}$	$Q_S = 48 \pm 1.1\ f^{0.37\pm0.07}$	0.25–6.31

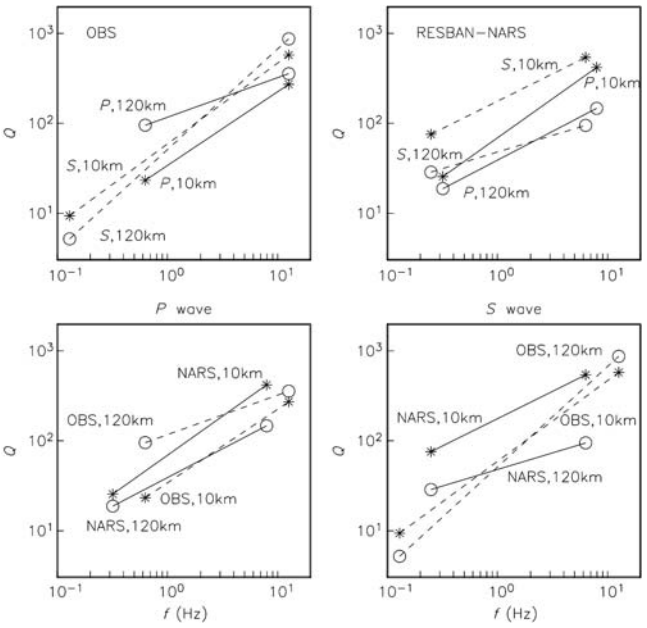

Figure 18. Summary of Q results listed in Table 2. Upper frames compare Q-frequency curves obtained for P (solid lines) and S (dashed lines) waves for source–station paths within the GoC (upper left) and for wavepaths traveling to the margins (upper right). The lines with asterisks and circles in the extremes of the lines indicate that Q was determined using data in the 10–120 km and 120–220 km distance range, respectively. Lower frames compare Q-frequency curves obtained for P waves (lower left) and for S waves (lower right) using data from OBS stations (dashed lines) and from the NARS-RESBAN stations (solid lines).

wave changes in the amplitudes decay at different distance ranges due to complex crustal and seafloor structure. We also observe that the inflection points of the different attenuation functions occur at different distances, suggesting that the geometrical spreading may depend on frequency and distance. We use these attenuation functions to estimate the quality factor Q and the geometrical spreading of both P and S waves. We found that Q increases with frequency for both waves following the relationship $Q = Q_0 f^a$. The estimates of Q obtained using OBS records for the interval between 10 and 120 km indicate that P waves attenuate more than S waves ($Q_P = 34f^{0.82}$, $Q_S = 59f^{0.90}$) for frequencies between 0.6 and 12.6 Hz; for the 120–220 km interval, however, S waves attenuate more than P waves ($Q_P = 117f^{0.44}$, $Q_S = 51f^{1.12}$). The estimates of Q obtained using NARS-Baja and RESBAN records within 10–120 km indicate that P waves attenuate more than S waves ($Q_P = 69f^{0.87}$, $Q_S = 176f^{0.61}$) at frequencies between 0.3 and 6.3 Hz, and similarly, for the 120–220 km interval ($Q_P = 39f^{0.64}$, $Q_S = 48f^{0.37}$). The low values of Q_0 for S waves obtained in this study from the OBS records agree with the low value expected for seismically active regions with young lithosphere (Sipkin and Jordan, 1980; Jin *et al.*, 1985), as occurs in other regions like the South Pacific rise.

To infer possible attenuation mechanisms to explain the observed values of Q, we calculated the Q_P/Q_S ratio (Fig. 17) and found that for most of the frequencies analyzed (0.6–12.6 Hz) for the OBS stations $Q_P < Q_S$ in the upper part of the crust, indicating that the rocks must be partially saturated. This finding also suggests that the crust and upper mantle along the plate boundary within the GoC is an area with many faults, fluid-filled pores, and molten rock. For longer wavepaths (120–220 km) $Q_P > Q_S$, probably due to the increase of temperature with depth. This is consistent with OBS locations deployed near the spreading centers where heat flow is higher and Q must be lower. The GoC is a rift system, formed from the extension process of the lithosphere that is associated with the rise of the asthenosphere, cortical thinning, and increased heat flow (Segor and Burke, 1978; Keen, 1985). In the southern GoC, Lizarralde *et al.* (2007) observed differences in rifting style and magmatism, from wide rifting with minor synchronous magmatism to narrow rifting in magmatically robust segments. On the other hand, when we calculate the Q_P/Q_S ratio for the NARS-Baja and RESBAN stations at frequencies between 0.3 and 6.3 Hz, $Q_S > Q_P$, which suggests that scattering (e.g., Hough and Anderson, 1988) must be an important attenuation mechanism that controls the amplitude decay with distance of the body waves that propagate in the Baja California Peninsula region.

Data and Resources

The seismograms used in this paper were recorded by stations of the RESBAN seismic array. Data from this network can be requested from the second author of this paper. Some plots were made using the Generic Mapping Tools (www.soest.hawaii.edu/gmt, last accessed April 2014; Wessel and Smith, 2009). Data from the SCOOBA OBS network can be obtained from the Incorporated Research Institutions for Seismology (IRIS) Data Management Center (www.iris.edu; last accessed October 2013).

Acknowledgments

The operation of the RESBAN network has been possible thanks to the financial support of the Mexican National Council for Science and Technology (CONACYT; projects CB-2011-01-165401[C0C059], G33102-T, and 59216). We are also grateful for the technical assistance given by Antonio Mendoza and Arturo Pérez Vertti. The first author benefited from a fellowship provided by CONACYT between August 2011 and August 2013. We also thank the financial support given by the Earth Science Division of Centro de Investigación Científica y de Educación Superior de Ensenada (CICESE) to write this paper. The authors also thank the anonymous reviewers, Associate Editor Martin Chapman, and Editor-in-Chief Diane Doser, who helped us to improve the manuscript. The SCOOBA OBS network was supported by the U.S. National Science Foundation.

References

Anderson, J. G., and R. Quaas (1988). The Mexico earthquake of September 19, 1985: Effect of magnitude on the character of strong ground motion: An example from the Guerrero, Mexico strong motion network, *Earthq. Spectra* **4,** 635–646.

Aragón-Arreola, M., and A. Martin-Barajas (2007). Westward migration of extension in the northern Gulf of California, Mexico, *Geology* **35,** 571–574, doi: 10.1130/G23360A.1 (PA: 58685).

Atwater, T. (1989). Plate tectonics history of the northeast Pacific and western North America, in *The Eastern Pacific Ocean and Hawaii*, E. L. Winterer, D. M. Hussong, and R. W. Decker (Editors), Geology of North America, Geological Society of America, Boulder, Colorado, 499–521.

Atwater, T., and J. Stock (1998). Pacific-North America plate tectonics of the Neogene southwestern United States: An update, *Int. Geol. Rev.* **40,** 375–402.

Axen, G. J., and M. J. Fletcher (1998). Late Miocene–Pleistocene extensional faulting, northern Gulf of California, Mexico and Salton Trough, California, *Int. Geol. Rev.* **40,** 217–244.

Axen, G. J., M. Grove, D. Stockli, O. M. Lovera, D. A. Rothstein, J. M. Fletcher, K. Farley, and P. L. Abbott (2000). Thermal evolution of Monte Blanco dome: Low-angle normal faulting during Gulf of California rifting and late Eocene denudation of the eastern Peninsular ranges, *Tectonics* **19,** 197–212.

Bennett, S., M. Oskin, and A. Iriondo (2007). Transition from Proto-Gulf extension to transtension, coastal Sonora, Mexico, *Eos Trans. AGU* **88,** 23.

Canas, J. A., and B. J. Mitchell (1978). Lateral variation of surface-wave anelastic attenuation across the Pacific, *Bull. Seismol. Soc. Am.* **68,** 1637–1650.

Castro, R. R., J. G. Anderson, and S. K. Singh (1990). Site response, attenuation and source spectra of *S* waves along the Guerrero, Mexico, subduction zone, *Bull. Seismol. Soc. Am.* **80,** 1481–1503.

Castro, R. R., H. Fabriol, M. Bour, and B. Le Brun (2003). Attenuation and site effects in the region of Guadeloupe, Lesser Antilles, *Bull. Seismol. Soc. Am.* **93,** 612–626.

Castro, R. R., M. R. Gallipoli, and M. Mucciarelli (2004). An attenuation study in southern Italy using local and regional earthquakes recorded by the seismic network of Basilicata, *Ann. Geofisc.* **47,** 1597–1608.

Curray, J. R., D. G. More, K. Kelts, and G. Einsele (1982). Tectonics and geological history of the passive continental margin at the tip of Baja California, *Initial reports of the Deep Sea Drilling Project*, Vol. 64, U. S. Government, Printing Office, Washington D. C. 1089–1116.

DeMets, C., and T. H. Dixon (1999). New kinematic models for Pacific-North America motion from 3 Ma to present, I: Evidence for steady motion and biases in the NUVEL-1A model, *Geophys. Res. Lett.* **26,** 1921–1924.

DeMets, C., R. G. Gordan, and D. F. Argus (2010). Geologically current plate motions, *Geophys. J. Int.* **181,** 1–80.

Fenby, S. S., and R. G. Gastil (1991). Geologic-tectonic map of the Gulf of California and surrounding areas, in *The Gulf and Penninsular Provinces of the Californias*, J. P. Dauphin and B. T. Simoneit (Editors), Vol. 47, American Association of Petroleum Geologist, 79–83.

Fletcher, J. M., and L. Munguía (2000). Active continental rifting in southern Baja California, Mexico: Implications for plate motion partitioning and the transition to seafloor spreading in the Gulf of California, *Tectonics* **19,** 1107–1123.

González-Fernández, A., J. J. Dañobeitia, L. A. Delgado-Argote, F. Michaud, D. Cordoba, and R. Bartolomé (2005). Mode of extension and rifting history of upper Tiburón and upper Delfín basins, northern Gulf of California, *J. Geophys. Res.* **110,** no. B01313, doi: 10.1029/2003JB002941.

Haberland, C., and A. Rietbrock (2001). Attenuation tomography in the western central Andes: A detailed insight into the structure of a magmatic arc, *J. Geophys. Res.* **106,** 11,151–11,167.

Hasegawa, H. S. (1985). Attenuation of *Lg* waves in the Canadian Shield, *Bull. Seismol. Soc. Am.* **75,** 1569–1582.

Hough, S. E., and J. G. Anderson (1988). High-frequency spectra observed at Anza, California: Implications for *Q* structure, *Bull. Seismol. Soc. Am.* **78,** 692–707.

Jin, A., T. Cao, and K. Aki (1985). Regional change of coda *Q* in the oceanic lithosphere, *J. Geophys. Res.* **90,** 8651–8659.

Johnston, D. H., M. N. Toksoz, and A. Timur (1979). Attenuation of seismic waves in dry and saturated rocks: II. Mechanisms, *Geophysics* **44,** 691–711.

Karig, D. E., and W. Jensky (1972). The Proto-Gulf of California, *Earth Planet. Sci. Lett.* **17,** 169–174.

Keen, C. E. (1985). The dynamics of rifting: Deformation of the lithosphere by active and passive driving mechanisms, *J. Geophys. Res.* **88,** 527–538.

Langston, C. A. (1977). Corvallis, Oregon, crustal and upper mantle receiver structure from teleseismic *P* and *S* waves, *Bull. Seismol. Soc. Am.* **67,** 713–724.

Lizarralde, D., G. J. Axen, H. E. Brown, J. M. Fletcher, A. González-Fernández, A. J. Harding, W. S. Holbrook, G. M. Kent, P. Paramo, and F. Sutherland (2007). Variation in styles of rifting in the Gulf of California, *Nature* **448,** 466–469.

Martin-Barajas, A. (2000). Volcanismo y extensión en la Provincia extensional del Golfo de California, *Boletín de la Sociedad Geológica Mexicana.* **53,** 72–83 (in Spanish).

Menke, W. (1984). *Geophysical Data Analysis: Discrete Inverse Theory*, Academia Press, New York, 1–260.

Mitchell, B. J., L. W. Leite, Y. K. Yu, and R. B. Hermann (1976). Attenuation of Love and Rayleigh waves across the Pacific at periods between 15 and 110 seconds, *Bull. Seismol. Soc. Am.* **68,** 1189–1202.

Nagy, E. A., and J. M. Stock (2000). Structural controls on the continent–ocean transition in the northern Gulf of California, *J. Geophys. Res.* **105,** 16,251–16,269.

Nakamura, Y. (1989). A method for dynamic characteristics estimation of subsurface using microtremor on the ground surface, *Report Railway Tech. Research Institute*. 30, 25–33.

Oskin, M., J. Stock, and A. Martin-Barajas (2001). Rapid localization of Pacific-North America plate motion in the Gulf of California, *Geology* **29,** 459–462.

Plattner, C., R. Malservisi, T. H. Dixon, P. LaFemina, G. F. Sella, J. Fletcher, and F. Suarez-Vidal (2007). New constraints on relative motion between the Pacific plate and Baja California microplate (Mexico) from GPS measurements, *Geophys. J. Int.* **170,** 1373–1380.

Sato, H. (1984). Attenuation and envelope formation of three-component seismograms of small local earthquakes in randomly inhomogeneous lithosphere, *J. Geophys. Res.* **89,** 1221–1241.

Segor, A. M. C., and K. Burke (1978). Relative timing of rifting and volcanism on Earth and its tectonic implications, *Geophys. Res. Lett.* **5,** 419–421.

Singh, S. K., and R. B. Herrmann (1983). Regionalization of crustal coda *Q* in the continental United States, *J. Geophys. Res.* **88,** 527–538.

Sipkin, S. A., and T. H. Jordan (1980). Regional variation of *QScS*, *Bull. Seismol. Soc. Am.* **70,** 1071–1102.

Stock, J. M., and K. V. Hodges (1989). Pre-Pliocene extension around the Gulf of California and the transfer of Baja California to the Pacific plate, *Tectonics* **8,** 99–115.

Suárez-Vidal, F., R. Armijo, G. Morgan, P. Bodin, and R. G. Gastil (1991). Framework of recent and active faulting in Northern Baja California, in *The Gulf and Peninsular Province of the California*, J. P. Dauphin and B. R. T. Simoneit (Editors), American Association of Petroleum Geologists, Memoir, Vol. 47, 285–300.

Sumy, D. F., J. B. Gaherty, W. Y. Kim, T. Diehl, and J. A. Collins (2013). The mechanisms of earthquakes and faulting in the Southern Gulf of California, *Bull. Seismol. Soc. Am.* **103,** 487–506.

Thatcher, W., and N. J. Brune (1971). Seismic study of an oceanic ridge earthquake swarm in the Gulf of California, *Geophys. J. Astron. Soc.* **22,** 473–489.

Tsai, Y. B., and K. Aki (1969). Simultaneous determination of the seismic moment and attenuation of seismic surface waves, *Bull. Seismol. Soc. Am.* **59,** 275–287.

Wessel, P., and W. H. F. Smith (2009). *The Generic Mapping Tools (GMT) Version 4.5.0 Technical Reference & Cookbook*, SOEST/NOAA.

Winkler, K., and A. Nur (1979). Pore fluid and seismic attenuation in rock, *Geophys. Res. Lett.* **6,** 1–4.

Winkler, K. W., and A. Nur (1982). Seismic attenuation: Effects of pore fluids and frictional sliding, *Geophysics* **47,** 1–15.

Centro de Investigación Científica y de Educación Superior de Ensenada (CICESE)
División Ciencias de la Tierra
Departamento de Sismología
Carretera Tijuana-Ensenada No. 3918
22860 Ensenada, Baja California, México
cvidales@cicese.edu.mx
raul@cicese.mx
(C.A.V.-B., R.R.C., C.I.H.)

University of Southern California
Induced Seismicity Consortium
Mork Family Department of Chemical Engineering and Materials Science
925 Bloom Walk
Los Angeles, California 90089
danielle.sumy@gmail.com
(D.F.S.)

Lamont-Doherty Earth Observatory of Columbia University
61 Route 9W
Palisades, New York 10964
gaherty@LDEO.columbia.edu
(J.B.G.)

Woods Hole Oceanographic Institution
Department of Geology and Geophysics
266 Woods Hole Road
Woods Hole, Massachusetts 02543
jcollins@whoi.edu
(J.A.C.)

Manuscript received 8 January 2014;
Published Online 1 July 2014